



Full length article

Micro-plasticity in a fragile model binary glass

P.M. Derlet^{a,*}, R. Maaß^{b,c}^a Condensed Matter Theory Group, Paul Scherrer Institut, CH-5232 Villigen PSI, Switzerland^b Federal Institute of Materials Research and Testing (BAM), Unter den Eichen 87, Berlin 12205, Germany^c Department of Materials Science and Engineering, University of Illinois at Urbana Champaign, 1304 West Green Street, Urbana, IL 61801, USA

ARTICLE INFO

Article history:

Received 4 November 2020

Revised 21 December 2020

Accepted 18 February 2021

Available online 8 March 2021

Keywords:

Bulk metallic glasses

Plasticity

Residual strains

Molecular dynamics

ABSTRACT

Atomistic deformation simulations in the nominally elastic regime are performed for a model binary glass with strain rates as low as $10^4/s$ (corresponding to 0.01 shear strain per 1 μs). A strain rate dependent elastic softening due to a micro-plasticity is observed, which is mediated by thermally-activated localized structural transformations (LSEs). A closer inspection of the atomic-scale structure indicates the material response is distinctly different for two types of local atomic environments. A system spanning icosahedrally coordinated substructure responds purely elastically, whereas the remaining substructure admits both elastic and microplastic evolution. This leads to a heterogeneous internal stress distribution which, upon unloading, results in negative creep and complete residual-strain recovery. A detailed structural analysis in terms of local stress, atomic displacement, and SU(2) local bonding topology shows such microscopic processes can result in large changes in local stress and are more likely to occur in geometrically frustrated regions characterized by higher free volume and softer elastic stiffness. The thermally-activated LSE activity also mediates structural relaxation, and in this way should be distinguished from stress-driven shear transformation activity which only rejuvenates glass structure. The frequency of LSE activity, and therefore the amount of micro-plasticity, is found to be related to the degree to which the glassy state is relaxed. These insights shed atomistic light onto the structural origins that may govern recent experimental observations of significant structural evolution in response to elastic loading protocols.

© 2021 Acta Materialia Inc. Published by Elsevier Ltd.

This is an open access article under the CC BY license (<http://creativecommons.org/licenses/by/4.0/>)

1. Introduction

The amorphous solid is a material strongly out of equilibrium and very much dependent on its thermal and loading history [1,2]. Despite this, structural glasses have a robust and extended elastic regime [3], and a well defined and high yield stress [4,5], giving them real-world industrial and engineering applications. This robustness and reproducibility implies a strongly constrained microstructure and therefore a spatially-correlated structural disorder from which structural length-scales can emerge [6,7]. Such emergent structural heterogeneity, which is difficult to characterize experimentally, strongly influences the macroscopic plasticity of the amorphous solid [8–10].

Classical thermally-activated micro-plasticity during the nominally elastic region, offers direct insight into a class of fundamental excitations of the solid that exist also under zero-load conditions [11]. Signatures of such microplastic activity can, for example, be indirectly seen in micro-tensile experiments [12], creep

and damping [13,14], isostatic macroscopic loading [15–17], fatigue [18], or stress-relaxation experiments [18]. The attribute “indirect” is used here since deformation in the absence of resolvable shear-band formation, is revealed as either non-linear pre-yield behaviour, a permanent residual strain upon unloading, or an increase in the stored excess enthalpy. More specific examples are the rejuvenation and a local increase in nano-scale elastic heterogeneity after cyclic loading [18], or the residual creep strain after applying a constant load at low homologous temperature [15,16]. Such studies reveal changes in measurable quantities that imply structural changes which, within the precision of experiments, can hardly be resolved. This inability to track detailed structural changes can be somewhat overcome with novel scattering methods using both X-rays and/or electrons, where for example fluctuation microscopy inside a transition electron microscope [19] or speckle patterns from coherent X-ray scattering [20] can shed light on the atomic scale structural change or dynamics. The present authors pursued such an approach in very recent work by tracking the structural dynamics during nominally elastic loading [21] and during cryogenic protocols [22] the latter of which activate structural excitations underlying the Gamma-mode [23]. Both these ef-

* Corresponding author.

E-mail address: peter.derlet@psi.ch (P.M. Derlet).

forts reveal a rich and non-trivial signature of structural dynamics quantified with time-dependent relaxation times that hint towards thermally-activated microplastic processes heterogeneous in both space and time. However, the quantified signals remain an average of a large number of atoms, and a detailed picture of the spatio-temporal characteristics of individual structural excitations is lacking.

This is where atomistic simulations have for a long time played a pivotal role by providing model based understanding of the microscopic structure and processes of metallic glasses, with a primary focus on binary and ternary model glass systems. Such efforts strongly support the early ideas of Frank [24], Chaudhari and Turnbull [25] and Nelson [26,27], which asserted a short-range order dominated by 5-fold coordinated bonds characterized by localized structural motives with (or close to) an icosahedral symmetry. Indeed, the fraction of local icosahedral environments is a strong measure of the degree to which a glass is relaxed [28–34], and the constraints associated with their connectivity is one avenue to understand medium range order and the associated emergence of structural length-scales [34,35]. Simulation has also given fundamental insight into the underlying microscopic processes during stress-driven athermal plasticity, demonstrating that mechanisms which mediate the collective athermal macroscopic response are fundamentally local [36–38]. Such localized activity is compatible with early thermal plasticity theories [39,40] and their coarse-grained simulation implementations [41–46]. More recently, potential energy landscape (PEL) exploration methods also revealed a local picture for thermally-activated structural excitations under both zero [47–51] and applied load [52]—a result confirmed by finite temperature molecular dynamics simulations [31,32,53] suggesting the possibility of glass plasticity driven by thermal fluctuations at sufficiently long deformation time scales.

Here we employ finite temperature molecular dynamics at the micro-second timescale, to demonstrate that a well relaxed binary model glass system exhibits a robust elastic regime largely insensitive to any structural relaxation occurring during the elastic loading. We do this for a well known Lennard–Jones system [54], whose resulting glassy structure forms a percolative icosahedral network consisting of fragments of the C15 Laves phase [34]—a feature that material specific model systems also exhibit [55,56]. We consider deformation strain rates spanning four orders of magnitude, and find that apart from minor elastic softening, the elastic regime is largely insensitive to the considered timescales, even though at the lowest strain rate of $10^4/s$, significant thermally-driven structural relaxation and micro-plasticity occurs. Central to this insensitivity is a pre-existing percolative icosahedral network that elastically deforms, whilst the remainder of the material undergoes micro-plasticity, resulting in a heterogeneous material in terms of internal stress. Unloading results in a residual strain, with the resulting elastic back-stress of the icosahedral network causing thermally-driven negative creep that leads to full recovery of the residual strain at a timescale comparable to the initial deformation.

2. Simulation methodology

2.1. Choice of Lennard–Jones potential, 50:50 chemical composition and physical units

The binary Lennard–Jones (LJ) potential of Wahnström [54] has been used extensively in atomistic simulations of model binary glass systems [31–33,49,50,52–54,57,58] and is widely known as a model fragile glass former. Since it is a pair potential, it is unable to describe the unsaturated nature of the metallic bond, and therefore the quantitative aspects of material specific binary model alloys. For this, embedded atom [59] or second-moment [60] em-

pirical many-body potentials are needed. Despite this aspect, the potential captures the essential structural physics of bulk binary metallic glasses as for example CuZr, ZrNi, NiNb, HfCu, CaAl etc., and the competition between liquid-like and crystal-like bonds which is believed to underlie such metallic glasses and its medium range order [24,25,28,35]. It is emphasized that the extent to which a Laves type phase forms for a given annealing protocol and chemical composition will be material specific, and in this sense, the use of a simple LJ interaction will be qualitative. Fundamentally the justification for using only a pair potential lies in the scale of local density variations, which whilst important for characterizing the structural state of the isotropic amorphous solid, are too small to distinguish the explicit many-body aspect of the material specific potential. For systems in which there are large changes in coordination, such as that at a surface or an internal cavitation, such LJ potentials would not be able to capture the bond stiffening expected for a metal. These aspects have been discussed in more detail in Refs. [31–33,53].

The present work employs a 50:50 chemical composition of small to large atoms, which is the potential's eutectic composition, therefore producing a homogeneous undercooled liquid and a glass with little chemical segregation. The system consists of 32,000 atoms, which is sufficiently large to study the average effect of micro-plasticity occurring in the nominal elastic regime.

The LJ potential has the following form:

$$V_{ab}(r) = 4\varepsilon \left(\left(\frac{\sigma_{ab}}{r} \right)^{12} - \left(\frac{\sigma_{ab}}{r} \right)^6 \right) \quad (1)$$

where $\sigma_{22} = 5/6\sigma_{11}$ and $\sigma_{12} = \sigma_{21} = 11/12\sigma_{11}$ for the Wahnström parametrization. The atoms of type 1 may be considered as the larger atom type. The atomic masses of the two atom types are arbitrarily chosen such that $m_1/m_2 = 2$. For a molecular dynamics iteration, a time step of $0.002778\sigma_{11}\sqrt{m_1/\varepsilon}$ is used. The distance unit is taken as $\sigma = \sigma_{11}$ and the energy unit as ε , with stresses in the units of ε/σ^3 . For this work, the potential is truncated to a distance 2.5σ .

When metallic units (representative of say, CuZr) are taken for ε and σ , an MD time-step is of the order of a femto-second. Thus one billion MD iterations corresponds to approximately one micro-second. Throughout this paper, simulation times will be measured with respect to one billion MD iterations, which in turn is approximated as one micro-second. Absolute temperatures are expressed as an energy, $k_B T$, using a value of $k_B = 8.617 \times 10^{-5} \text{ eV/K}$ where ε is assumed to have units of electron-Volt.

2.2. Sample preparation and deformation simulations

The sample preparation protocol exploits an initial NVT ensemble to produce a glassy structure at a local minimum in the PEL [31–33,50,52]. This sample has undergone 2 micro-seconds of relaxation at $0.95T_f^{\text{NVT}}$. Here, T_f^{NVT} is the fictive glass transition temperature at which the quenched undercooled liquid first becomes a glass (see Ref. [53]). Fixed zero pressure NPT simulations are subsequently performed using a linear temperature annealing protocol to determine the new fictive glass transition temperature T_f^{NPT} . Here such NPT simulations allow for the volume to fluctuate isotropically. Earlier work demonstrated that the same structural state may be obtained using either NVT or NPT ensembles, or a combination of both [32]. The configuration at $0.8T_f^{\text{NPT}}$ is then used for the shear deformation and zero-load simulations. In the present work, all simulations are performed at a temperature of $0.8T_f^{\text{NPT}}$.

The NPT simple-shear deformation simulations are performed involving a fixed strain rate in the xy plane. Thus the system's volume may fluctuate isotropically as the xy strain is applied. Due to only isotropic volume fluctuations being allowed, and also the finite

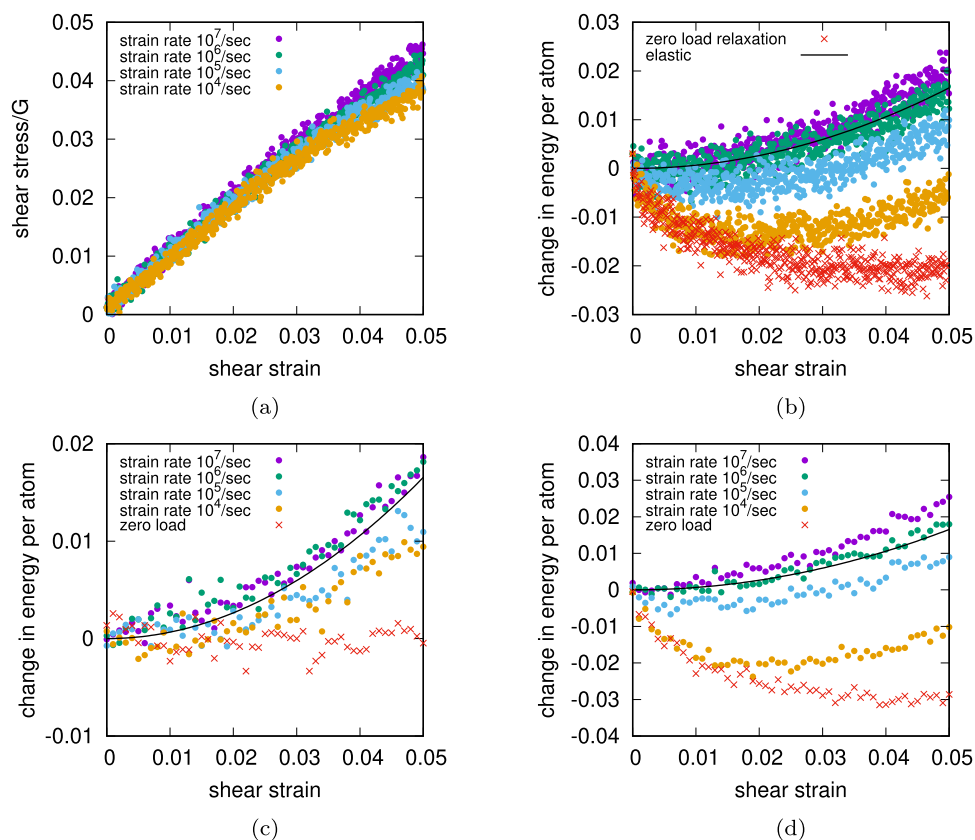


Fig. 1. Plot of (a) shear stress and (b) internal energy per atom as a function of shear strain for four orders of magnitude strain rate. The shear stress is divided by the shear modulus, G , measured at the highest strain-rate. In (b) the theoretical quadratic elastic response ($1/2G\gamma^2$) is also shown. Also shown is zero-load data, plotted with respect to the product of physical simulation time and the chosen strain rate of $10^4/s$. (c) and (d) show the corresponding average potential energy per atom as a function of shear strain for icosahedral and non-icosahedral coordinated atoms respectively. The same colour scheme is used in all panels.

size of the sample, the final sample will contain a small non-zero global shear stress corresponding to small shear strains of order 0.001. Over several micro-seconds these components may fluctuate in both sign and magnitude. Compared to thermal stress fluctuations and the typical applied stresses encountered in the present work they may be considered negligible. Their presence may be seen in the unloading curves of Fig. 2, the creep recovery simulations in Fig. 3, and the local stress analysis in Fig. 6.

3. Deformation simulations

3.1. Loading/unloading

Fig. 1a shows the shear stress-strain behaviour for strain-rates spanning four orders of magnitude. The highest strain-rate, $10^7/s$, is the typical nano-second deformation timescale considered in contemporary literature, whereas the lowest rate, $10^4/s$, involves one micro-second per 0.01 strain increment. The figure demonstrates an initial linear response for all strain rates, and at shear strains above 0.02–0.03, an increasing strain-rate effect is seen, which leads to a strain-rate dependent peak-stress response and a transition to plastic flow. This plastic regime will be considered in a forthcoming publication. A closer inspection of the initial linear response within the nominally elastic regime of strains up to 0.02, reveals an effective elastic softening that depends on strain rate. It will be demonstrated that this originates from thermally-activated micro-plasticity, and that the degree to which this occurs is intimately related to the degree of structural relaxation taking place during the deformation. This latter aspect turns out to be central to the observed strain rate dependence and may be seen by in-

specting the internal energy per atom as a function of shear-strain, Fig. 1b. Indeed, unlike Fig. 1a, a strong strain-rate dependence is now seen in the nominally elastic regime, where for the lowest strain-rate, the internal energy significantly decreases. For increasing strain-rates, the internal energy curves tend to approach the expected elastic response, $1/2G\gamma^2$, where G is the shear modulus derived from the 10^7 strain data (from strain values below 0.01), indicating that at the higher strain rates little structural relaxation is occurring during deformation. The red data set in Fig. 1b–d describe the temporal evolution of the configuration under zero-load, see Section 3.3, here plotted with respect to strain via $\dot{\epsilon} \times t$ for $\dot{\epsilon} = 10^4/s$.

Atoms are now classified into two groups as a function of the shear strain: those icosahedrally and non-icosahedrally coordinated using Vorop++ [61] within the OVITO software package [62]. For our well-relaxed sample, approximately 25% of the smaller atoms are icosahedrally coordinated. A connectivity analysis of the icosahedrally coordinated atoms reveals a dominant system spanning cluster consisting of connected fragments of C15 Laves backbone polyhedra. This is a known structural feature of the model LJ glass [34,57] and, generally, for isotropically bonded glassy systems [28,29,35,63–65]. Moreover, simulations have also revealed small C15 laves structures can emerge in a model CuZr glass [55,56,66] and the present LJ system [33]. For each group of atoms, an average potential energy per atom is calculated as a function of shear strain. These potential energies are obtained by performing a conjugate gradient relaxation to a local inherent state configuration to remove the thermal component (referred to as cg-quenched), and thus should be distinguished from the internal energies of Fig. 1a and b, which contain a thermal com-

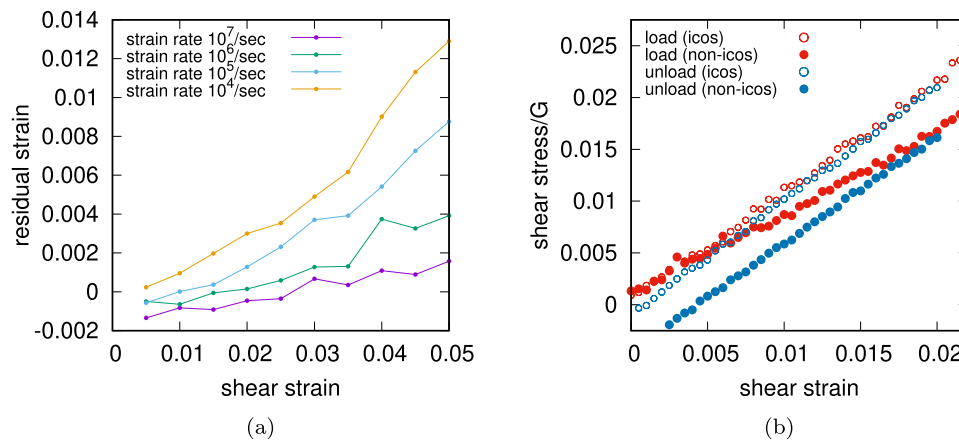


Fig. 2. (a) Residual strain upon unloading at different strains for the strain rates considered. (b) Average shear stress response of icosahedral and non-icosahedral regions during loading and unloading of the $10^4/s$ strain rate deformation. The elastic softening seen in the loading curve for the non-icosahedral regions in (b) mainly originates from micro-plasticity occurring at all stress/strain levels.

ponent. These icosahedral and non-icosahedral energies are shown respectively in Fig. 1c and d. Also shown in these figures is the expected elastic response, $1/2G\gamma^2$. Fig. 1c shows that the average energy of the icosahedral atoms follow more closely the elastic response at all shear-rates with only a weak dependence on strain rate, whereas Fig. 1d demonstrates that the non-icosahedrally coordinated atoms underlie the strain-rate dependent energy relaxation seen in Fig. 1b.

To explicitly reveal the presence and degree of the micro-plasticity occurring during the deformation shown in Fig. 1a, samples are unloaded to zero shear stress at various strains. The unloadings were performed at the upper strain rate of $10^7/s$, to ensure minimal structural relaxation and therefore maximal probing of the internal stress state at a particular strain. Fig. 2a displays the resulting residual strain and demonstrates that it is finite for all strains—even for strains below 0.02—and increases with decreasing strain rate. This indicates micro-plasticity is operative at all strains. To gain further insight into the origin of this micro-plasticity and how it might be related to the observed heterogeneous structural relaxation, the spatial load-bearing properties of the glassy structure are now investigated.

To determine the spatial origin of the evolving global shear stress, the virial stress $\sigma^{\mu\nu} = 1/(2V) \sum_{ij} F_{ij}^{\mu} r_{ij}^{\nu}$ (where \mathbf{F}_{ij} and \mathbf{r}_{ij} are the force and distance vectors between atoms i and j , V is the volume of the simulation cell, and the factor of $1/2$ is used to correct for double counting) is written as two terms, one involving a summation of i over icosahedrally coordinated atoms and the other over non-icosahedrally coordinated atoms. These two terms are used individually and divided respectively by the fraction of icosahedrally (Ω_I) and non-icosahedrally (Ω_{NI}) coordinated atoms. This allows determining the average local stress for each of the two atomic environments individually. Doing so, modifies the $1/V$ pre-factor to give a representative volume of the icosahedral and non-icosahedral regions, and therefore an estimate of the corresponding stresses. An average of the two quantities, weighted according to Ω_I and Ω_{NI} , gives the exact global stress of the system. Fig. 2b shows their evolution as a function of strain for the $10^4/s$ strain-rate sample derived from the corresponding cg-quenched inherent-state configurations. The data reveals that different shear stresses are carried by both regions of the material, with the non-icosahedral regions carrying a lower stress resulting in an effective elastic softening. From the corresponding unloading curve, this effective elastic softening is almost entirely due to the micro-plasticity responsible for the residual strain. Indeed, the gradient of the unloading curve, which directly probes

the true elastic shear modulus, is only slightly less than that of the icosahedral unloading curve supporting past simulations showing that the elastic stiffness modulus for the icosahedral region is somewhat higher than the global average [35,64,67]. The observed difference between the icosahedral and non-icosahedral stress responses seen in Fig. 2b decreases with increasing strain rate (data for other strain rates not shown), as suggested in Fig. 1c and d which show similar elastic responses at the higher strain rates. Thus the difference in shear stress between the two regions due to the underlying micro-plasticity, increases with decreasing strain rate, and is therefore the origin of the effective elastic softening seen in Fig. 1a.

3.2. Negative creep and strain recovery

The picture which therefore emerges is that, upon loading, the micro-plasticity occurring within the non-icosahedrally coordinated regions facilitates a reduction in stress (and energy) within these regions. Thus, upon unloading, a back-stress develops and produces the residual strains seen in Fig. 2a. The unloaded sample therefore experiences a heterogeneous internal shear stress distribution in which the icosahedral regions are under a positive shear stress and the non-icosahedral regions are under a negative shear stress, which together result in a net-zero shear stress. The observation that an increasing residual strain is observed with decreasing strain rate is strong evidence for thermally-activated micro-plasticity. If this is indeed the case, the unloaded heterogeneous micro-structure should experience negative creep, with the non-icosahedral regions facilitating micro-plasticity to reduce the negative stress which in turn will reduce the positive stress of the non-icosahedral regions, homogenizing the internal stress to eventually exhaust the negative creep. This has the experimental implication that time-dependent strain recovery may be present after a constant force experiment within the nominally elastic regime, evidence of which can be found in Refs. [13,17]. The present work refers to the strain recovery as “negative creep” since the non-icosahedral regions undergoing micro-plasticity are under negative load upon unloading (see Fig. 6b and related discussion in Section 4.1) and that we wish to distinguish this phenomenon from anelasticity which is often associated with reversible plasticity at the microscopic scale due to the removal of load.

Fig. 3 displays the resulting shear strain evolution (measured directly from the shear distortion of the simulation cell) as a function time of samples unloaded at a shear strain of 0.02 obtained at the two slowest strain rates (a) $10^5/s$ and (b) $10^4/s$. The NPT sim-

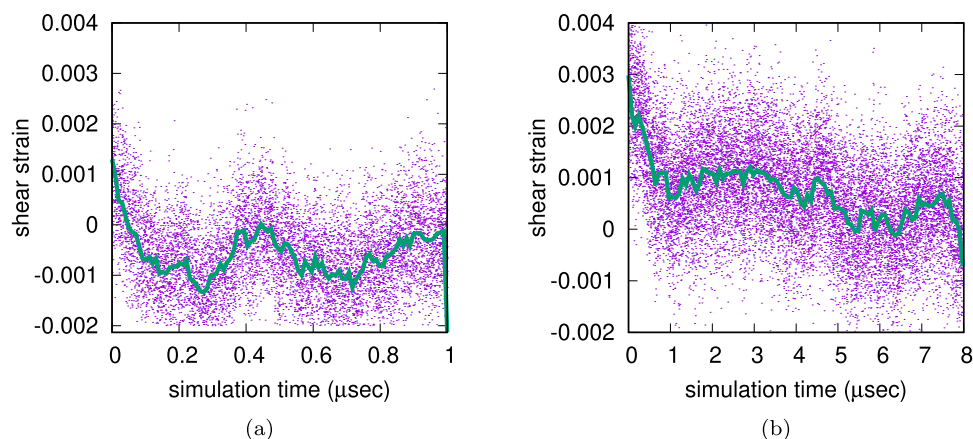


Fig. 3. Strain recovery evolution of samples unloaded at a shear strain of 0.02 for the $10^4/s$ and $10^5/s$ strain rates. The green solid curves indicate smoothed data. (For interpretation of the references to colour in this figure legend, the reader is referred to the web version of this article.)

ulations are performed at $0.8T_f^{NPT}$ using an additional zero shear stress barostat in the x - y plane. At $t = 0$ the data begins with an initial residual strain of approximately 0.001 and 0.003 for the respective strain rates, $10^5/s$ and $10^4/s$, as seen in Fig. 2a. For the $10^5/s$ loading to 0.02 the residual strain rapidly drops and by 100 nano-seconds begins fluctuating around a negative value of approximately 0.0005 at a time scale of order 200 nano-seconds. For the $10^4/s$ loading to 0.02 the residual strain also drops to a fluctuating value, now after several micro-seconds. In this case the fluctuations occur at the micro-second timescale. Thus in both cases, negative creep is indeed observed leading to strain recovery at a timescale larger but of similar order to the timescales associated with the deformation to 0.02 shear strain. The observed strong strain rate dependence on the strain recovery timescale is related to the degree to which the unloaded structures are relaxed and will be discussed in more detail in Section 5.

3.3. Comparison to zero-load evolution

The observations that (1) significant structural relaxation occurs during deformation at low enough strain rates, (2) this occurs in non-icosahedral regions which also undergo a reduction in shear, (3) residual strain exists upon unloading indicating micro-plasticity and (4) negative creep is seen resulting in recovery towards the pre-loading geometry, all point towards a strong thermally-activated micro-plasticity component.

Because of the inherently non-equilibrium nature of the glass structure, structural relaxation under zero-load also occurs via the thermal activation of microscopic scale processes. These localized structural changes are mediated by localized structural excitations (LSE). LSEs, can be observed in atomistic simulations at finite temperature within the dynamical heterogeneities of the under-cooled liquid [68–73], and also well below the glass transition temperature of the amorphous solid both [31,33,50,53]. They involve a core region in which atoms rearrange, often in a string-like fashion in which one atom replaces the position of a neighbouring atom. This localized activity is accommodated by a far-field Eshelby strain field which has a similar energy-scale as the LSE core [52]. Thermally-activated LSEs should be distinguished from athermally stress-driven shear transformation zones (STZs) [36–38,74] arising from inflections in the PEL, giving core structures significantly more localized than that of LSEs. Such STZs only occur during loading at sufficiently high stress, do not entail micro-plasticity at low strains [87], and lead to rejuvenation of the glassy structure through destruction of icosahedral content—see Ref. [75].

These considerations motivate the questions also eluded to in the introduction: (i) are there differences between the structural relaxation occurring under load and the relaxation processes that would normally occur under zero load? and (ii) would such zero-load structural relaxation be related to the thermally-activated micro-plasticity observed in Fig. 1?

To investigate the nature of structural relaxation without load, isothermal simulations are performed for 5 micro-seconds at zero fixed pressure and at $0.8T_f^{NPT}$, starting with the initial configuration used for the loading simulations. The cohesive energy per atom as a function of time is shown in Fig. 4a showing significant structural relaxation has occurred over the time scale of 5 micro-seconds. Such data may also be plotted as a function of $\dot{\epsilon} \times t$, giving a more direct indication of the structural relaxation occurring under zero load at the timescale associated with a particular strain achieved during deformation at a given strain-rate. Fig. 4b plots the zero-load relaxation data with respect to $\dot{\epsilon} \times t$ for the $10^4/s$ and $10^5/s$ strain rates, and the corresponding data of the deformation simulations with the elastic energy contribution ($1/2G\gamma^2$) removed. The curves show that the structural relaxation is similar. The zero load data is also shown in Fig. 1b–d (again as a function of $\dot{\epsilon} \times t$ for the $10^4/s$), which demonstrates that when the zero-load data is partitioned into icosahedral and non-icosahedral contributions—as under load, the non-icosahedral regions exhibit the bulk of the relaxation with the icosahedral regions experiencing minimal relaxation (see Fig. 1c and d). These simulations demonstrate the important result that in terms of energy decrease, very similar relaxation occurs for both zero load and during (and indeed somewhat beyond) the initial nominally elastic loading.

This structural relaxation is quantified in Fig. 5, which plots the evolution of the icosahedral content during loading as a function of shear strain for all strain rates. The data has been corrected for a general decrease in icosahedral content as a function of shear strain. This smooth reduction in icosahedral content, which is reversible upon unloading, also exists in purely athermal deformation and originates from the Voronoi based detection algorithm not being able to identify some strongly strained local icosahedral environments. For the highest $10^7/s$ strain rate, Fig. 5 shows that the corrected icosahedral content slightly decreases at strains beyond 0.02, indicating weak rejuvenation and a likely reason for why the energy per atom increases more rapidly than that expected from elasticity (see Fig. 1b and d). Such rejuvenation suggests the onset of athermal plasticity mediated by STZs [75]. For the two intermediate strain rates, the icosahedral content remains approximately constant. However for the $10^4/s$ strain rate, the icosahedral content increases until a strain of 0.01–0.02, and then plateaus at higher

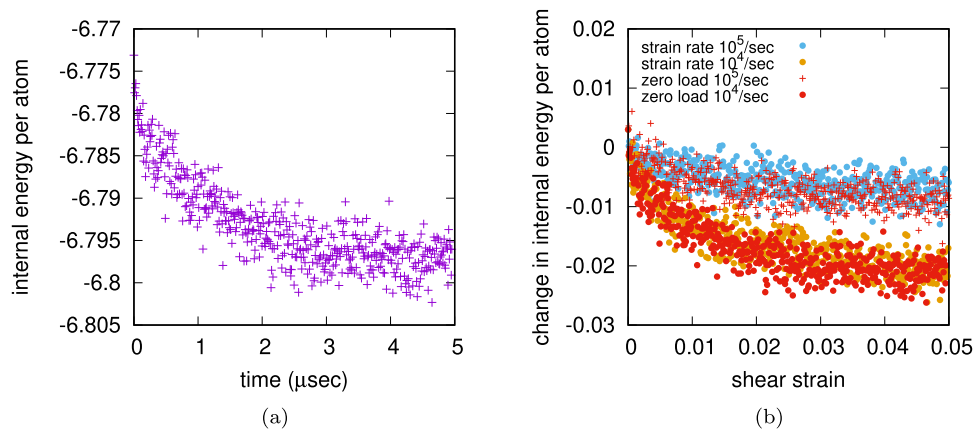


Fig. 4. (a) Plot of internal energy evolution of zero-load sample as a function of time. (b) Plot of internal energy evolution during loading minus the elastic energy component compared to the zero load internal energy evolution shown in (a), plotted as a function of $\dot{\epsilon} \times t$.

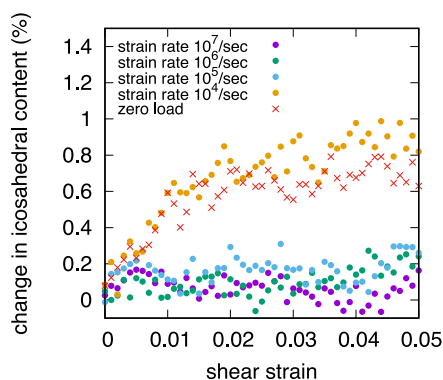


Fig. 5. (a) Icosahedral content as a function of strain, spanning 4 orders of magnitude in strain rate. Zero-load data is also shown as a function of the product of physical simulation time and the chosen strain of $10^4/s$.

strains. Also shown is the icosahedral evolution for the zero-load sample plotted as a function of $\dot{\epsilon} \times t$ for the $10^4/s$ strain rate, displaying a similar evolution in icosahedral content. Thus the initial rise in icosahedral content is due to the initial transient relaxation regime seen in both zero-load and loading simulations (Fig. 4).

Returning to questions (i) and (ii), structural evolution in terms of energy relaxation is similar for a zero or finite applied shear stress, with both being mediated by thermally-activated LSE activity. For the case of an applied load, the LSE activity clearly results

in a net shear stress reduction within the non-icosahedral regions. This connection between the degree of structural relaxation and degree of micro-plasticity will be discussed in Section 5.

4. Microscopic structural analysis

4.1. Local stress measure distribution

The results of the loading and unloading simulations reveal a developing internal stress heterogeneity that correlates with the icosahedral and non-icosahedral atomic environments. How is this stress heterogeneity manifested at the local microscopic level? Insight into this question may be seen by rewriting the expression for the global stress as

$$\sigma^{\mu\nu} = \frac{1}{2V} \sum_{ij} F_{ij}^{\mu} r_{ij}^{\nu} = \frac{1}{2NV_{\text{atom}}} \sum_{ij} F_{ij}^{\mu} r_{ij}^{\nu} = \frac{1}{N} \sum_i \sigma_i^{\mu\nu}, \quad (2)$$

where N is the number of atoms and V_{atom} is the average volume per atom. $\sigma_i^{\mu\nu}$ should be viewed as a measure of atom i 's contribution to the global stress, where the average value gives the global stress. It may also be seen as an estimate of the actual local atomic stress.

Fig. 6a displays a histogram of σ_i^{xy} for the zero-load (initial sample, the sample loaded to 0.02 shear strain at the strain rate of $10^4/s$, and the subsequently unloaded sample to approximately zero xy shear stress. The distributions are shown for the icosahedral and non-icosahedral atom classes. For the zero-load and unloaded samples, the distributions are centered at approximately

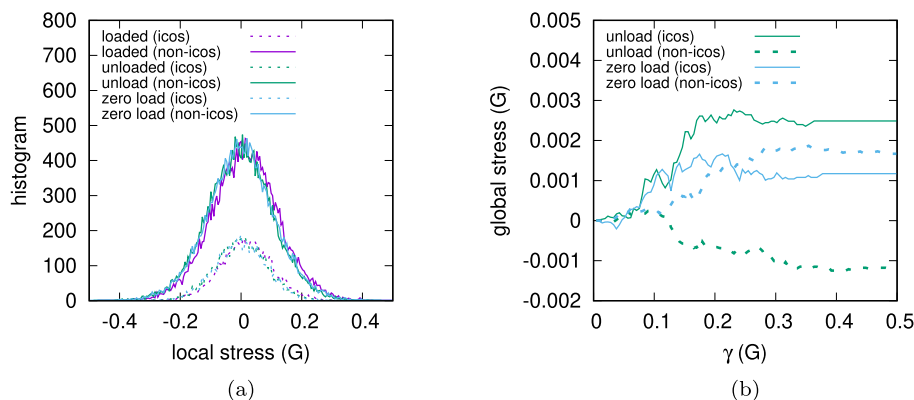


Fig. 6. (a) Histograms of the local shear-stress measure for the sample loaded to 0.02 shear strain at a strain rate of $10^4/s$, the unloaded and zero load (initial prior to loading) sample. The distributions are shown for both the icosahedral and non-icosahedral atoms. (b) The total global shear stress as a function of a local stress integration limit $\pm\gamma$ for the zero load and unloaded samples (see Section 4.1).

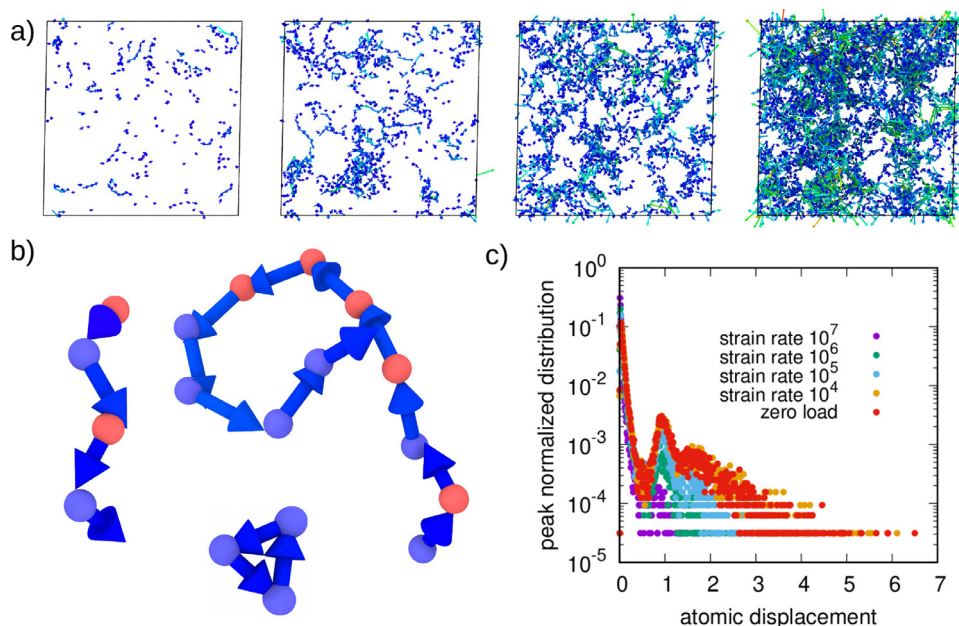


Fig. 7. (a) Atomic displacement maps showing the LSE mediated structural activity between the configuration prior to loading and at 0.02 strain for the strains rates $10^7/s$, $10^6/s$, $10^5/sec$, and $10^4/s$ corresponding to the time intervals Δt of 2.0 ns, 20.0 ns, 200.0 ns and 2 μs . (b) Examples of individual LSE activity consisting of string-like sequences of atomic displacements. (c) Van Hove spatial correlation function $G(r, \Delta t)$ associated with the configurations used in (a). Data associated with the zero-load sample is also shown for $\Delta t = 2 \mu s$.

zero, whereas for the loaded sample the distribution is shifted by approximately $0.02G$. Inspection of the figure reveals a bandwidth of shear stresses that is significantly larger than the applied stresses considered in the present work, and of a general form which is the same for both classes of atoms. Indeed, for all three samples, the most probable regions of the distributions are well described by a Gaussian, for which the width is $0.159G$ for the non-icosahedral data and $0.128G$ for the icosahedral data. For the zero-load and unloaded data the Gaussian centers are close to zero, whereas for the loaded sample, the centers are at $0.014G$ and $0.020G$.

Fig. 6b shows how the global averages of the icosahedral and non-icosahedral regions are obtained in terms of the distributions shown in Fig. 6a. This is done for the zero-load and unloaded sample by performing the summation in Eq. (2) but only including terms within the range $\pm\gamma$, and plotting the summation as a function of γ . Fig. 6b demonstrates that for small values of γ , which includes only the most probable part of the distribution, the global stress remains quite small. Deviations away from this begin in the tails of the distribution (below values of approximately the full-half-width-maximum), leading to the clear differences in the stress states of the icosahedral and non-icosahedral regions of the unloaded sample. On the other hand, the zero-load sample shows comparable values for the two classes of atoms, albeit at a clearly non-zero value of the global shear stress. This again reflects the fluctuating stress state of our finite sample, discussed in Section 2.2.

The results of this section indicate that the stress heterogeneity associated with the icosahedral and non-icosahedral regions manifests itself in differences in the local atomic stress distributions, where the distribution is consistently narrower for the icosahedral regions. On the other hand, the average stress difference of these regions originates from large, but rare, local stress contributions at the tails of these distributions. This result suggests that much of the internal stress state of the material remains inactive, with only certain regions undergoing structural change associated with relaxation and/or micro-plasticity.

4.2. Localized structural excitations

The present data, indicates that a similar thermally-activated relaxation scenario occurs for both zero- and finite-load conditions. Fig. 7a plots the atomic displacement between the sample prior to loading and the sample at 0.02 strain for the four considered strain rates, corresponding to respective time intervals of 2.0 ns, 20.0 ns, 200.0 ns and 2 μs . The displacement vectors are corrected for affine distortion due to the global shear strain. Only displacements above 0.6σ are visualized. The panels clearly show increased structural activity during the loading to 0.02 as a function of decreasing strain rate. The displacements may be characterized as consisting of an increasing number of localised structural rearrangements with respect to decreasing strain rate. Indeed, inspection of individual re-arrangements reveal them to be the LSEs seen under zero load in past work [31,33,50,53]. Fig. 7b displays a number of such LSEs, showing the string-like extended atomic displacement sequence.

To quantitatively confirm this similarity in LSE structure, atomic displacements occurring between a time interval, Δt , are binned to obtain the Van Hove self-correlation function, $G(r, \Delta t) = \langle \delta(r - |\mathbf{r}_i(\Delta t) - \mathbf{r}_i(0)|) \rangle$, a quantity that is experimentally accessible using coherent photon correlation spectroscopy methods [21]. Fig. 7c plots the resulting correlation function obtained from the configurations prior to load and at a shear strain of 0.02 for all strain rates corresponding to a respective Δt of 2.0 ns, 20.0 ns, 200.0 ns and 2 μs . All correlation functions demonstrate two structural features: (1) a narrow peak whose maximum is close to zero with a width that spans displacements below the characteristic bond-length (here $\sim 1\sigma$), and (2) a peak at this characteristic bond-length which exhibits an exponential tail at larger displacements. The intensity of this latter peak increases with decreasing strain rate (increasing Δt). Fig. 7c also includes the Van Hove self-correlation function at zero-load for $\Delta t = 2 \mu s$ which due to a similar time interval may be directly compared to the 10^4 strain rate data, and which demonstrates a close overlap with the lowest strain rate. A similar overlap can be seen

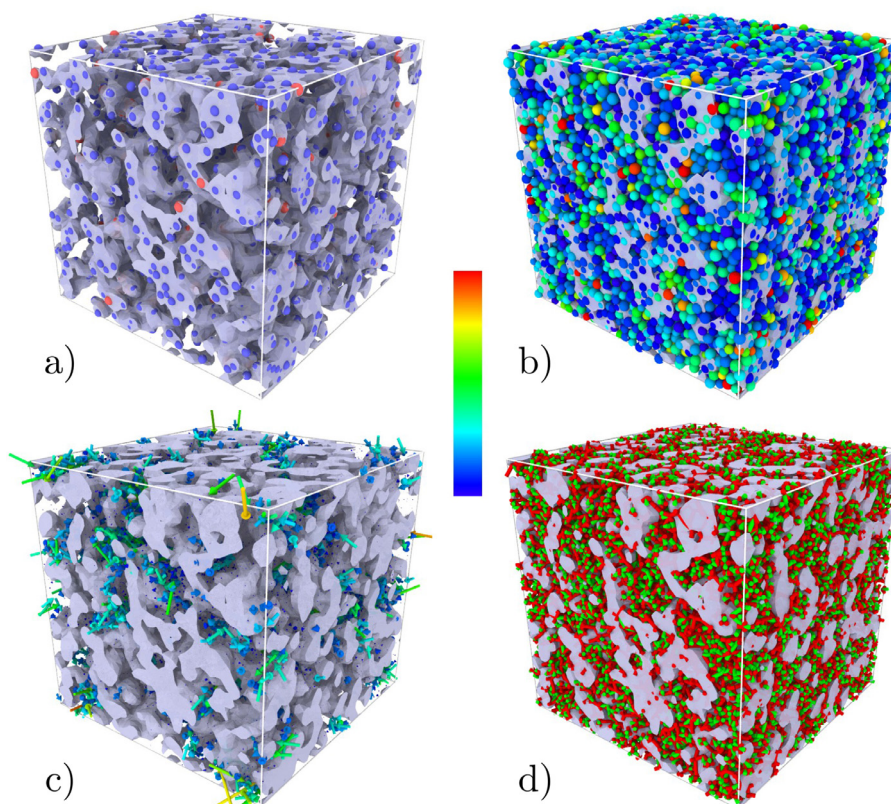


Fig. 8. Visualization of initial structure in which (a) only atoms that are icosahedrally coordinated are shown (blue/red represent the small/large atoms), (b) all atoms are shown and coloured according to their change in Von Mises stress at 0.02 shear strain (where blue represents no change and red represents a change of greater than $0.4G$), (c) the displacement vectors between the initial configuration and the configuration at 0.02 shear strain are shown. Each vector is coloured according to its magnitude (where blue represents zero magnitude and red a magnitude of 6σ), (d) the initial disclination network in which green represents 4-fold bonds and red 6-fold bonds (See Ref. [34]). In all figures the visualized surface mesh encloses the atoms of (a). For (b) and (c) intermediate stresses and displacement magnitudes can be determined by the central colour bar.

for the higher strain rates when using the appropriate Δt (not shown).

In addition, comparison of the second peak associated with bond-length displacements, for the different strain rates show a similar overall structure—the main effect being that the intensity of the second peak increases with decreasing strain rate. A similar effect is seen for the correlation functions derived from the icosahedral and non-icosahedral regions of the sample. Here the atomic displacement statistics is again similar in form, but the intensity of the second peak is larger for the non-icosahedral regions. Thus, between the two spatial regions, only the level of activity is different not the nature of the activity, where for the $\Delta t = 2 \mu\text{s}$ correlation functions, only $\approx 4\%$ of icosahedrally coordinated atoms were involved in bond-length scale displacements, whereas for non-icosahedrally coordinated atoms it was $\approx 16\%$. This is compatible with past work demonstrating that for the undercooled liquid, as the temperature approaches the glass transition regime, mobility is significantly arrested for icosahedral coordinated atomic environments [76,77].

More generally, the character of thermally-activated LSE activity is the same, whether under load or not, where the second peak is associated with LSE core atom bond length (or greater) displacements. The observed exponential tail at larger distances is a characteristic of collective behaviour and conjectured to be a universal feature of the glass transition regime [78]. The present work extends this property to the thermally-activated LSE processes below the glass transition regime. The sub-bond-length displacements associated with the first peak correspond to the accommodating LSE Eshelby strain field indicating an intrinsic landscape of small bar-

rier energies which has been viewed as a collective generalization of rattling-in-the-cage excitations [79].

4.3. Spatial visualization

To visualize the spatial region defined by the icosahedrally coordinated atoms, the initial configuration is shown in Fig. 8a, which displays only the icosahedral atoms. Here, blue/red atoms correspond to the small/large atoms. A surface mesh encloses these atoms. Inspection of the figure demonstrates the dominance of the smaller atom and that the connected cluster of atoms is system spanning. Fig. 8b plots all atoms, now coloured according to the change in local Von Mises stress arising for 0.02 strain, with the yellow-orange-red atoms indicating large changes in stress of the order of $0.4G$. These mainly occur in the non-icosahedral regions and are relatively rare amongst largely inactive regions. This reflects the strongly heterogeneous changes in internal stress at the atomic scale, revealed in Section 4.1. Fig. 8c now displays the atomic displacement vectors between this initial configuration and the configuration at 0.02 shear strain for the slowest strain rate $10^4/\text{s}$. The displacement vectors are coloured according to their magnitude. Detailed inspection of this figure reveals bond-length displacements mainly happen within the non-icosahedral regions. These displacements occur via multiple LSE activity as discussed in Section 4.2 (see also Fig. 7). Some non-icosahedral regions are also displacement-inactive, reflecting the strongly heterogeneous nature of LSE activity.

To gain further insight into the structural nature of the non-icosahedral regions, a local $SU(2)$ topological analysis is performed,

following a similar approach as that done in Ref. [34]. This procedure, uses a modified radical Voronoi tessellation procedure to determine the bond-order of each nearest neighbour pair, defined as the number of common neighbours of the two atoms. The relevance of this description of glassy structure has its origins in Refs [24–27], where the liquid like 5-fold bond order represents the minimally frustrated packing of atoms around the bond. As a result, this bond is referred to as a defect free bond. On the other hand, 4-fold and 6-fold bonds are not minimally frustrated atomic packings, and are referred to as defected bond orders. From this perspective, the icosahedral environment is an atom with 12 defect-free bonds and thus represents a minimally frustrated short-range-order structure. The discrete symmetries of the icosahedral point group combined with the rotational invariance of a sphere, result in homotopy group which can be represented by the SU(2) algebra whose elements correspond to the breaking of symmetry along the six 5-fold symmetry axes of the icosahedron [26,27,34]. This breaking of symmetry results in 4-fold and 6-fold defect bonds around an atom which obey certain combinations and orientations describable by the SU(2) algebra, as do the corresponding 4-fold and 6-fold disclinations constructed from connected lines of such defect bonds. When visualized, disclinations represent lines along which the 5-fold local symmetry of the icosahedron has been broken. The rules of the SU(2) algebra can be seen as constraints on the local bond order geometry and for example result in the impossibility of terminating an isolated 4-fold or 6-fold disclination. The recent work of Ref. [34] shows that a large proportion of atomic environments of the model LJ binary glass presently considered follow the rules dictated by the SU(2) algebraic structure. An OVITO python modifier which calculates and visualizes the resulting disclination network is freely available via GitHub [80].

Fig. 8d displays the disclination network constructed from showing only the green (4-fold) and red (6-fold) bonds. The direction along the disclination line represents an axis on which the 5-fold local icosahedral symmetry is broken either by a 4-fold or 6-fold symmetry. Inspection of the figure reveals that within the icosahedral region, mainly 6-fold bonds occur indicating Frank-Kasper [81] SU(2) topologies, whereas in the non-icosahedral regions both 4-fold and 6-fold disclinations exist indicating so-called Nelson SU(2) topologies [34]. These later topologies entail disclination nodes in which both green and red disclinations intersect according to the rules of the underlying SU(2) algebra (see Refs. [26,27]). Their presence indicates highly bond-frustrated environments. Indeed the work of Ref. [34] found that minimization of 4-fold disclination content indicates a reduction in the bond frustration of the glassy structure (See Fig. 5 of Ref. [34] and the related discussion) and that such environments are characterized by higher free volume and locally soft (possibly negative) elastic stiffness shear moduli, both of which facilitate LSE activity [34]. This latter result gives insight into why the icosahedral regions have a higher elastic stiffness [35,67] than the non-icosahedral regions – the defect-free regions are minimally frustrated, corresponding to more stable bonding environments which in turn are more rigid (higher curvature in the PEL with respect to local affine distortions, see Sec. IIIC4 in Ref. [34] for a related discussion). The observation that the non-icosahedral regions, are more frustrated, elastically softer regions containing increased free-volume is compatible with the increased thermally-activated structural relaxation and micro-plasticity occurring in these regions.

5. Discussion

The present atomistic simulation work, which employs samples relaxed and deformed at the micro-second timescale, has revealed the emergence of thermally-activated micro-plasticity within the

nominally elastic regime at strains less than 0.02, as the strain rate reduces. The degree of micro-plasticity is heterogeneously distributed within the micro-structure, being active in regions characterized by no icosahedral content. The thermally-activated local structural excitations (LSEs) underlying these deformation mechanisms also result in the relaxation of the glassy structure within the non-icosahedral regions. Such heterogeneous LSE activity also occurs without load, but without the developing internal stress heterogeneity, suggesting a link between thermally-activated plasticity and structural relaxation. This has important consequences for micro-plasticity, since thermally-activated structural relaxation under zero-load (which results in increased icosahedral content) becomes increasingly arrested as the structure relaxes, so must the structural relaxation and micro-plasticity occurring under load. Together these results point towards a classical thermal-activation picture of plasticity, as was applied by Spaepen [39], Argon [40] and Bulatov and Argon [41], which all rely on the stochastic occurrence of thermally-activated localised plastic events, biased by the applied load. These works, in turn, exploit the seminal work of Eshelby [82].

Most generally, a change in energy due to thermal activation of an LSE may be written as a sum of a core contribution, E_{core} , and an Eshelby elastic energy contribution [82]:

$$1/2V_0\varepsilon_T^{\mu\nu}(\sigma_T^{\mu\nu} - \sigma_C^{\mu\nu} - \sigma_L^{\mu\nu}). \quad (3)$$

Here V_0 is the volume of the Eshelby inclusion appropriate for the LSE, $\sigma_T^{\mu\nu}$ and $\varepsilon_T^{\mu\nu}$ are the rigid far-field elastic stress and strain due to the Eshelby construction, $\sigma_C^{\mu\nu}$ is the correction due to internal relaxation around the Eshelby inclusion, and $\sigma_L^{\mu\nu}$ is the characteristic external stress at the LSE. Due to its strongly local character, E_{core} is expected to have a much weaker dependence on $\sigma_L^{\mu\nu}$ than the Eshelby contribution. Taking $\sigma_L^{\mu\nu}$ as a simple shear in the xy plane of magnitude σ , its contraction with $\varepsilon_T^{\mu\nu}$ gives $\varepsilon_T^{\mu\nu}\sigma_L^{\mu\nu} = 2\sigma\gamma_T\cos 2\theta_T$ and an energy which depends on the LSE's Eshelby shear-strain magnitude γ_T and orientation θ_T within the xy plane. A similar expression for the corresponding saddle-point energy may also be obtained [41] resulting in a barrier energy whose leading order stress dependence will be $\sim \sigma\gamma_T\cos 2\theta_T$, giving the general result that thermally-activated LSEs with a far-field strain signature that reduces the applied load (i.e. $\cos 2\theta_T < 0$) are more likely to occur, reducing the global elastic energy through the global plastic strain increment $\varepsilon_T^{\mu\nu}$ (here γ_T). This picture of a barrier energy dependent on the applied stress has been confirmed through ARTn simulations which investigated how particular barrier energies varied with load, finding that in terms of a shear load, LSE barrier energies would either increase or decrease depending on their far field shear-stress signature and whether or not it is compatible with the loading geometry [52]. Equivalently, the stress dependence of the barrier energy could be well characterized by a shear-stress activation volume which could be either positive or negative. Thus a shear loading geometry could either enhance or suppress the occurrence of a particular LSE. This work also demonstrated that the LSE barrier energy originates partially from the core region of the LSE (approximately 50%) and partially from the elastic energy of the accommodating strain field of the surrounding amorphous matrix.

The above heuristic picture of thermally-activated plasticity gives a simple reason as to why similar degrees of energy relaxation and displacement activity are seen when comparing the loaded sample to the zero-load sample—a certain degree of thermal activation will occur irrespective of the presence of an applied load. Under zero load, over time, this activity will result in structural relaxation with no net deformation of the sample. However with an applied load, thermal activity will be biased towards those LSEs which reduce the applied elastic load leading to micro-plasticity at all stresses within the nominally elastic regime of de-

formation and a corresponding elastic softening, as seen in Fig. 2b for the non-icosahedral region of the sample. The observation that this bias does not affect the degree of thermally-activated structural relaxation (over a given strain/time interval), infers that the glass structure is sufficiently complex to support a very large number of LSEs with a broad range of far-field strain signatures.

The heterogeneity in the level of activity of micro-plasticity within the icosahedral and non-icosahedral regions, has an analogue in the limit of athermal stress-driven localized plasticity. Extensive past atomistic simulation work probing the high-strain rate ($\geq 10^7/s$), low temperature, deformation regime has demonstrated suppressed shear transformation zone (STZ) activity within the icosahedral regions [75,83] (also see the review article, Ref. [84] and references therein.). On the other hand, STZ activity is found to be more favorable in non-icosahedral structural motives referred to as GUMs (geometrically unfavorable motives) [29]. More generally, these past works demonstrate an athermal plasticity whose features (increasing stress overshoot and strain localization in the flow regime with increasing icosahedral content) are dependent on the level of icosahedral content, which are in turn related to the specific composition and the degree of structural relaxation.

The effect of such structural heterogeneity on plasticity has also been investigated at temperatures close to the glass transition regime. In the work of Baumer and Demcowitz [85], which considered a model CuNb binary glass at a concentration away from its eutectic, and therefore with strong chemical segregation, the authors found a system-spanning icosahedral network at the interface between the regions rich in Cu and rich in Nb. This occurred at the the glass transition temperature regime, giving a strong analogy to the general phenomenon of gelation. Detailed analysis of their shear loading simulations performed at the glass transition temperature and at a strain rate of $10^9/s$ revealed the non-icosahedral regions (referred to as liquid-like) plasticised. This resulted in a characteristic cohesive energy that did not depend strongly on the applied strain, whereas the icosahedral network responded approximately elastically. Moreover, upon unloading, no residual strain was observed indicating the plastic processes within the liquid-like non-icosahedral regions were entirely reversible. The present work establishes a related phenomenon but at lower temperatures and slower strain rates. In particular, the significantly enhanced time scales enables the observation of recovery via classical thermally-activated micro-plasticity which we refer to as negative creep.

This is nicely demonstrated in Fig. 3, where time-dependent strain recovery (negative creep) proceeds after unloading. Due to the slow loading rate and the ability of the non-icosahedral network to admit thermally-activated structural micro-plasticity, an incompatibility stress (and therefore strain) between both structural components emerges upon unloading. The magnitude of the residual strain must, if true thermally-activated micro-plasticity occurs during loading, depend on temperature, strain rate, and the initial structural state of the glass (see below). These observations provide an atomistic understanding of various experimental observations of inelasticity and strain recovery after both static and cyclic loading conditions at stresses well below yielding [12–15,17], which typically are described with viscoelastic Kelvin–Voigt or Maxwell models. The applicability of such phenomenological laws to the here observed atomic-scale strain recovery at the micro-second time scale will be reported elsewhere.

The distinguishing feature of the presently observed thermally-activated micro-plasticity is its close coupling to structural relaxation and thus increased icosahedral content at the slowest strain rate (see Fig. 5). The situation is quite different in athermal plasticity for which STZ mediated activity results in the destruction of icosahedral content [75,86,87] and therefore rejuvenation of the

glass structure. Fig. 4a shows that the degree of isothermal structural relaxation significantly arrests after a few micro-seconds. Indeed, the initial faster transient relaxation processes have disappeared by two micro-seconds, which is the time taken for deformation to a strain of 0.02 for the strain rate $10^4/s$. On the other hand for the $10^5/s$ strain rate, these transient relaxation processes are still very much active at a strain of 0.02 (or equivalently a time scale of 200 nano-seconds). This gives a qualitative explanation for the large order-of-magnitude difference in strain recovery time scales for the 10^5 and $10^4/s$ strain rates (Fig. 3). Because of the significantly more relaxed sample and a corresponding reduction in the timescale for further relaxation for the slower strain rate sample, micro-plasticity is arrested resulting in a longer time until full strain recovery occurs. Equivalently, loading of a more relaxed sample, should result in less micro-plasticity, and therefore a reduced effective elastic softening and less residual strain upon unloading as that seen in Fig. 2. This latter aspect will be investigated in future work.

Thus the level of micro-plasticity activity is intimately connected to the degree to which the glassy structure is relaxed. This is compatible with micro-plasticity mainly occurring in non-icosahedral regions and icosahedral content being a direct measure of the degree of relaxation because of its minimally frustrated local geometry [34]. Past simulation work has demonstrated that as the glass transition regime is entered from the under-cooled liquid a icosahedral network is rapidly formed [28,29,34,35,57,63–65] which underlies the corresponding non-Arrhenius kinetic arrest [76,77], motivating the suggestion that the rate of structural ordering reflects the degree of fragility [88]. From this perspective, given a similar preparation protocol, more fragile isotropic glasses might generally entail lower levels of thermally-activated micro-plasticity at temperatures below the glass transition.

After the elastic energy component has been subtracted from the cohesive energy, the degree of energy relaxation of the loading and zero-load curves is quite similar for the lower strain rates (Fig. 4b). From this, and the observation of strain recovery, one might conclude that little relative rejuvenation occurs due to the micro-plasticity. Experimental changes in enthalpy due to rejuvenation occurring within the nominally elastic regime are typically a few 100 J/mol (see Refs. [15,16,89]) and can be as high as ~ 1 kJ/mol [23]. 100J/mol is approximately 0.001 eV per atom and assuming the LJ parameter ε is at the scale of one electron volt, detecting such relative energy changes in the simulation data becomes difficult because of the fluctuations associated with the finite size of the system. It is however encouraging that the present simulations could entail relative rejuvenation energies not much larger than this typical energy scale of 100 J/mol. In terms of absolute change (not relative to the zero-load sample) significant relaxation has of course occurred over the timescale of the deformation, which is certainly not the case during a typical experimental deformation. Inspection of Fig. 4b reveals a structural relaxation involving a reduction in energy of about 0.02ε per atom. This corresponds to ~ 2 kJ/mol when ε is taken as an electron volt, which is comparable to what is seen in the fast quenching of a ribbon [90]. Together, these aspects motivate future deformation simulations within the nominal elastic regime on more relaxed configurations. For example, the configuration at 5 μ s in Fig. 4a for which all μ sec transients have disappeared appears as an ideal candidate for such an endeavor. Such simulations could involve loading protocols such as that done in cyclic loading experiments [18,91], which have found that both the elastic and plastic mechanical properties can be altered. However, the precise structural mechanisms and experimental conditions to induce either relaxation or rejuvenation remain unclear [92].

Beyond a shear strain of 0.02, Fig. 1a indicates a greater strain rate dependence with an increased shear softening with decreasing

ing strain rate. In addition Fig. 2a shows that with respect to shear strain, this regime entails a more rapid increase of the residual strain upon unloading. These observations, at the micro-second timescale, could be a very early signature of the onset of plastic flow at the shear strain levels where bulk metallic glasses characteristically deform in experiments.

6. Concluding summary

The nominal elastic regime has been studied for a well known fragile model binary glass using strain rates spanning four orders of magnitude. The work finds:

1. a strain rate dependent elastic softening due to a micro-plasticity mediated by thermally-activated localized structural transformations (LSEs) which, upon unloading, results in a residual strain that fully recovers through negative creep at a time scale comparable to the initial loading.
2. such thermally-activated LSEs also occur under zero load, mediating general structural relaxation, and are less numerous in a system spanning region characterized by high icosahedral and negligible 4-fold disclination content, both of which reflect a minimally frustrated structure.
3. under load this minimally frustrated structure responds elastically, whereas the remainder of the structure experiences an elastic and micro-plastic response at all stress levels, leading to local elastic softening and the emergence of a heterogeneous internal stress distribution, whose thermally-activated homogenization upon unloading drives the observed strain recovery.
4. the frequency of occurrence of thermally-activated LSEs mediating the structural relaxation and micro-plasticity depends on the degree to which the glass structure is relaxed—the degree of micro-plasticity is therefore intimately linked to the level of frustration within the glassy structure.

Because of their thermal activation LSEs are different from shear transformation zones (STZ) which occur only under an applied load. Moreover, whilst STZs also result in intermittent micro-plasticity at higher elastic strains [87], they do so through rejuvenating the structure, whereas LSEs generally result in structural relaxation. These considerations should motivate new experiments on bulk metallic glasses that specifically probe the temperature, time and strain rate dependence of micro-plasticity and its relation to rejuvenation, as well as further atomistic simulations done at micro-second (and indeed the sub-millisecond) timescales. As pointed out in a recent overview article by the present authors [11], micro-plasticity probes the fundamental thermally-activated unit-scale plastic processes that are characteristic of the zero-load structural state. A proper understanding of these local processes is essential when entering the high-stress regime of collective phenomena that ultimately lead to rejuvenation, yield and plastic flow.

Declaration of Competing Interest

The authors declare that they have no known competing financial interests or personal relationships that could have appeared to influence the work reported in this paper.

Acknowledgements

The present work was supported by the [Swiss National Science Foundation](#) under grant no. 200021-165527.

References

- [1] Y. Sun, A. Concustell, A.L. Greer, Thermomechanical processing of metallic-glasses: extending the range of the glassy state, *Nat. Rev. Mater.* 1 (2016) 16039.
- [2] T.C. Hufnagel, C.A. Schuh, M.L. Falk, Deformation of metallic glasses: recent developments in theory, simulations, and experiments, *Acta Mater.* 109 (2016) 375.
- [3] L. Tian, Y.-Q. Cheng, Z.-W. Shan, J. Li, C.-C. Wang, X.-D. Han, J. Sun, E. Ma, Approaching the ideal elastic limit of metallic glasses, *Nat. Commun.* 3 (2012) 609.
- [4] W.F. Wu, Y. Li, C.A. Schuh, Strength, plasticity and brittleness of bulk metallic glasses under compression: statistical and geometric effects, *Philos. Mag.* 88 (2008) 71–89.
- [5] J.S. Harmon, M.D. Demetriou, W.L. Johnson, K. Samwer, Anelastic to plastic transition in metallic glass-forming liquids, *Phys. Rev. Lett.* 99 (2007) 135502.
- [6] F. Zhu, A. Hirata, P. Liu, S. Song, Y. Tian, J. Han, T. Fujita, M. Chen, Correlation between local structure order and spatial heterogeneity in a metallic glass, *Phys. Rev. Lett.* 119 (2017) 215501.
- [7] C. Liu, R. Maass, Elastic fluctuations and structural heterogeneities in metallic glasses, *Adv. Funct. Mater.* 28 (2018) 1800388.
- [8] N. Wang, J. Ding, F. Yan, M. Asta, R.O. Ritchie, L. Li, Spatial correlation of elastic heterogeneity tunes the deformation behavior of metallic glasses, *npj Comput. Mater.* 4 (2018) 19.
- [9] Q. An, K. Samwer, M.D. Demetriou, M.C. Floyd, D.O. Duggins, W.L. Johnson, W.A. Goddard, How the toughness in metallic glasses depends on topological and chemical heterogeneity, *Proc. Nat. Acad. Sci.* 113 (2016) 7053–7058.
- [10] F. Zhu, H.K. Nguyen, S.X. Song, D.P.B. Aji, A. Hirata, H. Wang, K. Nakajima, M.W. Chen, Intrinsic correlation between [beta]-relaxation and spatial heterogeneity in a metallic glass, *Nat. Commun.* 7 (2016) 11516.
- [11] R. Maass, P.M. Derlet, Micro-plasticity and recent insights from intermittent and small-scale plasticity, *Acta Mater.* 143 (2018) 338–363.
- [12] Y. Wu, H.X. Li, G.L. Chen, X.D. Hui, B.Y. Wang, Z.P. Lu, Nonlinear tensile deformation behavior of small-sized metallic glasses, *Scr. Mater.* 61 (6) (2009) 564–567.
- [13] A. Castellero, B. Moser, D.I. Uhlenhaut, F.H.D. Torre, J.F. Loffler, Room-temperature creep and structural relaxation of Mg-Cu-Y metallic glasses, *Acta Mater.* 56 (15) (2008) 3777–3785.
- [14] J.C. Ye, J. Lu, C.T. Liu, Q. Wang, Y. Yang, Atomistic free-volume zones and inelastic deformation of metallic glasses, *Nat. Mater.* 9 (8) (2010) 619–623.
- [15] S.-C. Lee, C.-M. Lee, J.-W. Yang, J.C. Lee, Microstructural evolution of an elastically compressed amorphous alloy and its influence on the mechanical properties, *Scr. Mater.* 58 (7) (2008) 591–594.
- [16] A.L. Greer, Y.H. Sun, Stored energy in metallic glasses due to strains within the elastic limit, *Philos. Mag.* 96 (16) (2016) 1643–1663.
- [17] T.J. Lei, L.R. DaCosta, M. Liu, W.H. Wang, Y.H. Sun, A.L. Greer, M. Atzmon, Microscopic characterization of structural relaxation and cryogenic rejuvenation in metallic glasses, *Acta Mater.* 164 (2019) 165–170.
- [18] P. Ross, S. Kuechemann, P.M. Derlet, H. Yu, W. Arnold, P. Liaw, K. Samwer, R. Maass, Linking macroscopic rejuvenation to nano-elastic fluctuations in a metallic glass, *Acta Mater.* 138 (2017) 111–118.
- [19] P. Zhang, J.J. Maldonis, Z. Liu, J. Schroers, P.M. Voyles, Spatially heterogeneous dynamics in a metallic glass forming liquid imaged by electron correlation microscopy, *Nat. Commun.* 9 (1) (2018) 1129.
- [20] B. Ruta, E. Pineda, Z. Evenson, Relaxation processes and physical aging in metallic glasses, *J. Phys.* 29 (50) (2017) 503002.
- [21] A. Das, P.M. Derlet, C. Liu, E.M. Dufresne, R. Maass, Stress breaks universal aging behavior in a metallic glass, *Nat. Commun.* 10 (1) (2019) 5006.
- [22] A. Das, E.M. Dufresne, R. Maass, Structural dynamics and rejuvenation during cryogenic cycling in a Zr-based metallic glass, *Acta Mater.* 196 (2020) 723–732.
- [23] S. Kuechemann, R. Maass, Gamma relaxation in bulk metallic glasses, *Scr. Mater.* 137 (2017) 5–8.
- [24] C. Frank, Super cooling of liquids, *Proc. R. Soc. A* 215 (1952) 43–46.
- [25] P. Chaudhari, D. Turnbull, Structure and properties of metallic glasses, *Science* 199 (1978) 11–21.
- [26] D.R. Nelson, Liquids and glasses in spaces of incommensurate curvature, *Phys. Rev. Lett.* 50 (1983) 982–985.
- [27] D.R. Nelson, Order, frustration, and defects in liquids and glasses, *Phys. Rev. B* 28 (1983) 5515–5535.
- [28] H.W. Sheng, W.K. Luo, F.M. Alamgir, J.M. Bai, E. Ma, Atomic packing and short-to-medium-range order in metallic glasses, *Nature* 439 (2006) 419–425.
- [29] J. Ding, Y.-Q. Cheng, E. Ma, Full icosahedra dominate local order in Cu₆₄Zr₃₄ metallic glass and supercooled liquid, *Acta Mater.* 69 (2014) 343–354.
- [30] J. Ding, E. Ma, Computational modeling sheds light on structural evolution in metallic glasses and supercooled liquids, *npj Comput. Mater.* 3 (2017) 9.
- [31] P.M. Derlet, R. Maass, Thermally-activated stress relaxation in a model amorphous solid and the formation of a system-spanning shear event, *Acta Mater.* 143 (2018) 205–213.
- [32] P.M. Derlet, R. Maass, Local volume as a robust structural measure and its connection to icosahedral content in a model binary amorphous system, *Materialia* 3 (2018) 97–106.
- [33] P.M. Derlet, R. Maass, Emergent structural length scales in a model binary glass—the micro-second molecular dynamics time-scale regime, *J. Alloys Compd.* 821 (2020) 153209.
- [34] P.M. Derlet, Correlated disorder in a model binary glass through a local SU(2) bonding topology, *Phys. Rev. Mater.* 4 (2020) 125601.
- [35] E. Ma, Tuning order into disorder, *Nat. Mater.* 14 (2015) 547–552.
- [36] M.L. Falk, J.S. Langer, Dynamics of viscoplastic deformation in amorphous solids, *Phys. Rev. E* 57 (1998) 7192–7205.
- [37] C. Maloney, A. Lemaître, Subextensive scaling in the athermal, quasistatic limit of amorphous matter in plastic shear flow, *Phys. Rev. Lett.* 93 (2004) 016001.

- [38] M.J. Demkowicz, A.S. Argon, Liquidlike atomic environments act as plasticity carriers in amorphous silicon, *Phys. Rev. B* 72 (2005) 245205.
- [39] F. Spaepen, Microscopic mechanism for steady-state inhomogeneous flow in metallic glasses, *Acta Metall.* 25 (1977) 407–415.
- [40] A.S. Argon, Plastic deformation in metallic glasses, *Acta Metall.* 27 (1979) 47–58.
- [41] V.V. Bulatov, A.S. Argon, A stochastic model for continuum elasto-plastic behavior. I. Numerical approach and strain localization, *Model. Simul. Mater. Sci. Eng.* 2 (1994) 167–184.
- [42] V.V. Bulatov, A.S. Argon, A stochastic model for continuum elasto-plastic behavior. II. A study of the glass transition and structural relaxation, *Model. Simul. Mater. Sci. Eng.* 2 (1994) 185–202.
- [43] V.V. Bulatov, A.S. Argon, A stochastic model for continuum elasto-plastic behavior. III. Plasticity in ordered versus disordered solids, *Model. Simul. Mater. Sci. Eng.* 2 (1994) 203–222.
- [44] E.R. Homer, C.A. Schuh, Mesoscale modeling of amorphous metals by shear transformation zone dynamics, *Acta Mater.* 57 (2009) 2823–2833.
- [45] E.R. Homer, C.A. Schuh, Three-dimensional shear transformation zone dynamics model for amorphous metals, *Model. Simul. Mater. Sci. Eng.* 18 (2010) 065009.
- [46] L. Li, E.R. Homer, C.A. Schuh, Shear transformation zone dynamics model for metallic glasses incorporating free volume as a state variable, *Acta Mater.* 61 (2013) 3347–3359.
- [47] D. Rodney, C. Schuh, Distribution of thermally activated plastic events in a flowing glass, *Phys. Rev. Lett.* 102 (2009) 235503.
- [48] D. Rodney, C.A. Schuh, Yield stress in metallic glasses: the jamming-unjamming transition studied through Monte Carlo simulations based on the activation-relaxation technique, *Phys. Rev. B* 80 (2009) 184203–184212.
- [49] P. Koziatek, J.-L. Barrat, P.M. Derlet, D. Rodney, Inverse Meyer–Neldel behavior for activated processes in model glasses, *Phys. Rev. B* 87 (2013) 224105.
- [50] S. Swayamjyoti, J.F. Löffler, P.M. Derlet, Local structural excitations in model glasses, *Phys. Rev. B* 89 (2014) 224201.
- [51] Y. Fan, T. Iwashita, T. Egami, Energy landscape-driven non-equilibrium evolution of inherent structure in disordered material, *Nat. Commun.* 8 (2017) 15471.
- [52] S. Swayamjyoti, J.F. Löffler, P.M. Derlet, Local structural excitations in model glass systems under applied load, *Phys. Rev. B* 93 (2016) 144202.
- [53] P.M. Derlet, R. Maass, Thermal processing and enthalpy storage of an amorphous solid: a molecular dynamics study, *J. Mat. Res.* 32 (2017) 2668.
- [54] G. Wahnström, Molecular-dynamics study of a supercooled two-component Lennard–Jones system, *Phys. Rev. A* 44 (1991) 3752–3764.
- [55] J. Zemp, M. Celino, B. Schönfeld, J.F. Löffler, Icosahedral superclusters in $\text{Cu}_{64}\text{Zr}_{36}$ metallic glass, *Phys. Rev. B* 90 (2014) 144108.
- [56] J. Zemp, M. Celino, B. Schönfeld, J.F. Löffler, Crystal-like rearrangements of icosahedra in simulated copper-zirconium metallic glasses and their effect on mechanical properties, *Phys. Rev. Lett.* 115 (2015) 165501.
- [57] U.R. Pedersen, T.B. Schröder, J.C. Dyre, P. Harrowell, Geometry of slow structural fluctuations in a supercooled binary alloy, *Phys. Rev. Lett.* 104 (2010) 105701.
- [58] D. Rodney, A. Tanguy, D. Vandembroucq, Modeling the mechanics of amorphous solids at different length scale and time scale, *Model. Simul. Mater. Sci. Eng.* 19 (2011) 083001.
- [59] M.S. Daw, M. Baskes, Embedded-atom method: derivation and application to impurities, surfaces, and other defects in metals, *Phys. Rev. B* 29 (1984) 6443–6453.
- [60] M.W. Finnis, J.E. Sinclair, A simple empirical N-body potential for transition metals, *Philos. Mag.* A 50 (1984) 45–55.
- [61] C.H. Rycroft, Voro++: a three-dimensional Voronoi cell library in C++, *Chaos* 19 (2009) 041111.
- [62] A. Stukowski, Visualization and analysis of atomistic simulation data with OVITO—the open visualization tool, *Model. Simul. Mater. Sci. Eng.* 18 (2010) 015012.
- [63] H. Jónsson, H.C. Andersen, Icosahedral ordering in the Lennard–Jones liquid and glass, *Phys. Rev. Lett.* 60 (1988) 2295–2297.
- [64] M. Wakeda, Y. Shibutani, Icosahedral clustering with medium-range order and local elastic properties of amorphous metals, *Acta Mater.* 58 (2010) 3963–3969.
- [65] R. Soklaski, Z. Nussinov, V. Markov, K.F. Kelton, L. Yang, Connectivity of icosahedral network and a dramatically growing static length scale in Cu–Zr binary metallic glasses, *Phys. Rev. B* 87 (2013) 184203–184210.
- [66] R.R. Ryltsev, B.A. Klumov, N.M. Chitchev, K.Y. Shunyaev, Cooling rate dependence of simulated $\text{Cu}_{64.5}\text{Zr}_{35.5}$ metallic glass structure, *J. Chem. Phys.* 145 (2016) 034506.
- [67] Y.Q. Cheng, A.J. Cao, E. Ma, Correlation between the elastic modulus and the intrinsic plastic behavior of metallic glasses: the roles of atomic configuration and alloy composition, *Acta Mater.* 57 (2009) 3253–3267.
- [68] C. Donati, J.F. Douglas, W. Kob, S.J. Plimpton, P.H. Poole, S.C. Glotzer, String-like Cooperative Motion in a Supercooled Liquid, *Phys. Rev. Lett.* 80 (1998) 2338–2341.
- [69] T.B. Schröder, S. Sastry, J.C. Dyre, S.C. Glotzer, Crossover to potential energy landscape dominated dynamics in a model glass-forming liquid, *J. Chem. Phys.* 112 (2000) 9834–9849.
- [70] Y. Gebremichael, M. Vogel, S.C. Glotzer, Particle dynamics and the development of string-like motion in a simulated monoatomic supercooled liquid, *J. Chem. Phys.* 120 (2004) 4415–4427.
- [71] M. Vogel, B. Doliwa, A. Heuer, S.C. Glotzer, Particle rearrangements during transitions between local minima of the potential energy landscape of a binary Lennard–Jones liquid, *J. Chem. Phys.* 120 (2004) 4404–4414.
- [72] D. Chandler, J.P. Garrahan, Dynamics on the way to forming glass: bubbles in space-time, *Annu. Rev. Phys. Chem.* 61 (2010) 191–217.
- [73] T. Kawasaki, A. Onuki, Dynamics of thermal vibrational motions and stringlike jump motions in three-dimensional glass-forming liquids, *J. Chem. Phys.* 138 (2013) 12A514–12A519.
- [74] Y. Shi, M.L. Falk, Strain localization and percolation of stable structure in amorphous solids, *Phys. Rev. Lett.* 95 (2005) 095502.
- [75] Y.Q. Cheng, A.J. Cao, H.W. Sheng, E. Ma, Local order influences initiation of plastic flow in metallic glass: effects of alloy composition and sample cooling history, *Acta Mater.* 56 (2008) 5263–5275.
- [76] Y.Q. Cheng, H.W. Sheng, E. Ma, Relationship between structure, dynamics, and mechanical properties in metallic glass-forming alloys, *Phys. Rev. B* 78 (2008) 014207.
- [77] Y.Q. Cheng, E. Ma, H.W. Sheng, Alloying strongly influences the structure, dynamics, and glass forming ability of metallic supercooled liquids, *Appl. Phys. Lett.* 93 (2008) 111913.
- [78] P. Chaudhuri, L. Berthier, W. Kob, Universal nature of particle displacements close to glass and jamming transitions, *Phys. Rev. Lett.* 99 (2007) 060604.
- [79] M.P. Ciamarra, R. Pastore, A. Coniglio, Particle jumps in structural glasses, *Soft Matter* 12 (2016) 358–366.
- [80] See GitHub repository at <https://github.com/derlet/SU2>.
- [81] F.C. Frank, J.S. Kasper, Complex alloy structures regarded as sphere packings. I. Definitions and basic principles, *Acta Crystallogr.* 11 (1958) 184.
- [82] J.D. Eshelby, The determination of the elastic field of an ellipsoidal inclusion, and related problems, *Proc. R. Soc. A* 241 (1957) 376–396.
- [83] M. Wakeda, Y. Shibutani, S. Ogata, J. Park, Relationship between local geometrical factors and mechanical properties for Cu–Zr amorphous alloys, *Intermetallics* 15 (2007) 139–144.
- [84] Y.Q. Cheng, E. Ma, Atomic-level structure and structure-property relationship in metallic glasses, *Prog. Mater. Sci.* 56 (2011) 379–473.
- [85] R.E. Baumer, M.J. Demkowicz, Glass transition by gelation in a phase separating binary alloy, *Phys. Rev. Lett.* 110 (2013) 145502.
- [86] C.E. Lekka, A. Ibenskas, A.R. Yavari, G.A. Evangelakis, Tensile deformation accommodation in microscopic metallic glasses via subnanocluster reconstructions, *Appl. Phys. Lett.* 91 (2007) 214103.
- [87] K.-W. Park, C.-M. Lee, M. Wakeda, Y. Shibutani, M.L. Falk, J.C. Lee, Elastically induced structural disordering in amorphous alloys, *Acta Mater.* 56 (2008) 5440–5450.
- [88] N.A. Mauro, M. Blodgett, M.L. Johnson, A.J. Vogt, K.F. Kelton, A structural signature of liquid fragility, *Nat. Commun.* 5 (2014) 4616.
- [89] M. Zhang, Y.M. Wang, F.X. Li, S.Q. Jiang, M.Z. Li, L. Liu, Mechanical relaxation-to-rejuvenation transition in a Zr-based bulk metallic glass, *Sci. Rep.* 7 (2017) 625.
- [90] L. Battezzati, G. Riontino, M. Baricco, A. Lucci, F. Marino, A DSC study of structural relaxation in metallic glasses prepared with different quenching rates, *J. Non-Cryst. Solids* 61 (62) (1984) 877–882.
- [91] C.E. Packard, L.M. Witmer, C.A. Schuh, Hardening of a metallic glass during cyclic loading in the elastic range, *Appl. Phys. Lett.* 92 (2008) 171911.
- [92] C.M. Meylan, A.L. Greer, The effects of elastic cycling in nanoindentation of a metallic glass, *Philos. Mag.* 100 (2020) 3141–3154.